# Sugarcane Bagasse-Derived Activated Carbon as a Potential Material for Lead Ions Removal from Aqueous Solution and Supercapacitor Energy Storage Application

**Somyanonthanakun, W., Greszta, A., Roberts, A. J. & Thongmee, S**

**Published PDF deposited in Coventry University's Repository**

**Original citation:**
Somyanonthanakun, W, Greszta, A, Roberts, AJ & Thongmee, S 2023, 'Sugarcane Bagasse-Derived Activated Carbon as a Potential Material for Lead Ions Removal from Aqueous Solution and Supercapacitor Energy Storage Application', Sustainability, vol. 15, no. 6, 5566. https://doi.org/10.3390/su15065566

**DOI 10.3390/su15065566**
**ISSN 2071-1050**

**Publisher: MDPI**

**Copyright: © 2023 by the authors. Licensee MDPI, Basel, Switzerland. This article is an open access article distributed under the terms and conditions of the Creative Commons Attribution (CC BY) license (https:// creativecommons.org/licenses/by/ 4.0/)**

sustainability

MDPI

Article

# Sugarcane Bagasse-Derived Activated Carbon as a Potential Material for Lead Ions Removal from Aqueous Solution and Supercapacitor Energy Storage Application

**Wuttichai Somyanonthanakun [1], Agata Greszta [2], Alexander J. Roberts [2,*] and Sirikanjana Thongmee [1,*]**

[1] Department of Physics, Faculty of Science, Kasetsart University, Bangkok 10900, Thailand
[2] Clean Growth and Future Mobility, Coventry University, Coventry CV1 5FB, UK
* Correspondence: alexander.roberts@coventry.ac.uk (A.J.R.); fscisjn@ku.ac.th (S.T.)

**Abstract:** Sugarcane bagasse-based activated carbon (AC) was produced via a physical activation method using $CO_2$, to remove lead (Pb) ions from an aqueous solution. The physical and chemical properties of ACs were examined by scanning electron micrograph (SEM), Brunauer–Emmett–Teller (BET) surface area, and Fourier-transform infrared spectroscopy (FTIR) analysis. The effect of both pH and contact time on adsorption was studied via a batch process. Based on the BET results, we have identified that BET surface area and micropore volume decreased at the highest activation temperature, while the intensity of the functional groups increased when the activation temperature was raised. The adsorption isotherms were best fitted with the Langmuir equation, which was used to describe the adsorption process and to examine the adsorption mechanisms of Pb(II) on the AC. The maximum adsorption capacity of Pb(II) was 60.24 mg $g^{-1}$ with AC850. The adsorption kinetic study closely followed the pseudo-second order ($R^2 > 0.99$). AC has the potential to economically remove metal ions in the purification process of wastewater. AC850 was also utilized in the manufacture and testing of pouch cell supercapacitors to demonstrate the potential of the sugarcane bagasse family of materials in energy storage applications. The devices made with the unmodified, nonoptimized material used for Pb(II) sorption demonstrated high rate and power-energy characteristics (>50% capacitance retention with 10-fold increase in current density, 10 Wh $Kg^{-1}$ at 2500 W $Kg^{-1}$, active material mass) but there remains a need for further optimization, particularly the removal of oxygen functionality, to enhance lifetime and specific capacitance. This work demonstrated the potential for sugarcane bagasse carbons across environmental applications.

**Keywords:** sugarcane bagasse; activated carbon; lead removal; supercapacitors; energy storage

check for updates

**Citation:** Somyanonthanakun, W.; Greszta, A.; Roberts, A.J.; Thongmee, S. Sugarcane Bagasse-Derived Activated Carbon as a Potential Material for Lead Ions Removal from Aqueous Solution and Supercapacitor Energy Storage Application. *Sustainability* **2023**, *15*, 5566. https://doi.org/10.3390/su15065566

Academic Editor: Farooq Sher

Received: 28 February 2023
Revised: 14 March 2023
Accepted: 19 March 2023
Published: 22 March 2023

**Copyright:** © 2023 by the authors. Licensee MDPI, Basel, Switzerland. This article is an open access article distributed under the terms and conditions of the Creative Commons Attribution (CC BY) license (https://creativecommons.org/licenses/by/4.0/).

## 1. Introduction

Over the last few decades, activated carbons (ACs) have been widely used in pollution control processes and energy storage applications such as purification and separation processes [1–3], removal of toxic substances [4–7], gas storage [8,9], supercapacitors [10–14], wastewater treatment [15–19], etc. These applications require the same properties: high surface area and porosity, excellent adsorption capability, efficient electrical properties, eco-friendliness, low cost, and no secondary pollution. Recent technological advancements have shown many advantages for producing AC to meet the needs of commercial applications. The properties of ACs are dependent on the raw materials and the activation technology [20]. Technological developments have led to enhancements, such as pore structure and volume, surface areas, and improvements in surface chemistry, regarding functional groups and adsorption capacity [21,22].

In terms of the raw material for AC, researchers have increasingly sought to make it from waste materials produced by industry and agriculture. The use of waste by-products is advantageous because it is accessible and affordable. ACs can be prepared from many agricultural by-products that have a high carbon and low ash content, such as coconut

shells [23,24], rice husk [25,26], coffee residue [27], bamboo [28–30], pineapple crown waste [31], palm shell [32,33], and olive stones [34].

Generally speaking, there are two traditional methods to produce AC, namely, chemical activation and physical activation. Chemical activation involves a combination of single-step carbonization and activation by impregnating the raw material with dehydrating chemicals such as $H_3PO_4$, $ZnCl_2$, $K_2CO_3$, NaOH, or KOH then carbonizing it under an inert atmosphere at the desired temperature [35–37]. Using physical activation, as is widely used to produce AC for commercial application, the process is to carbonize the raw material and then place it within an oxidizing gas atmosphere of $CO_2$ [38], water steam [39], air, or some combination of these activating agents under a moderately high temperature (800–1100 °C) to improve the internal structure. The high adsorption performance of activated carbon is related to the porosity of the carbons. Therefore, carefully produced activated carbon materials have shown performance in the range to adsorb large amounts and various types of heavy metal adsorption and electrode material.

With ongoing economic growth, more pollutants than ever are being discharged into the environment. Heavy metals in the environment, such as lead, copper, zinc, chromium, cadmium, and mercury, can cause serious problems for nature and human health, with buildup in the food chain posing a threat to human wellbeing and the environment. In this study, removal of Pb(II) from water is considered. Pb(II) ions can be found in both soils and groundwater as a result of wastewater generated from increasing industrialization such as electroplating, leather tanning, metal finishing, textile industries, and the production of lead additives in gasoline [40]. The negative impacts associated with lead ion pollution can be addressed by processes including ion exchange [41], AC adsorption [42,43], membrane filtration [44,45], and chemical precipitation [46,47]. Currently, adsorption is considered to be one of the simplest and most effective technologies and AC is the most frequently used adsorbent. One of the core challenges of AC production is to create highly specific kinds of carbons that are well suited for specific industry applications.

A further environmental application for AC is in energy storage applications, such as in the electrodes of supercapacitor devices, utilizing extensive, tailored pore structures and surface area that can be tailored to various electrolytes.

This research aims to produce an economical AC using agricultural waste in the form of sugarcane bagasse, with physical activation using $CO_2$ to avoid further impurities derived from chemicals in the activation process [48].

The AC produced is investigated with the primary application of the removal of Pb(II) from water but with a secondary application as electrodes for supercapacitor energy storage devices. The adsorption capacity of Pb(II) ions from an aqueous solution was investigated, considering the effect of pH, contact time, and initial concentration of Pb(II), with fitting and calculation of kinetic models from adsorption isotherms. The AC optimized for Pb(II) adsorption was processed without further optimization into electrodes and assembled into organic electrolyte-based supercapacitor single-layer pouch cells (SLPs), illustrating the potential of the family of sugarcane bagasse-derived ACs across environmental applications.

This potential dual use of a single process and feedstock across environmental applications highlights the versatility of the AC produced and illustrates the potential of this industrial waste feedstock in two key areas of environmental sustainability: water clean-up and energy storage.

## 2. Materials and Methods

### *2.1. Preparation of Sugarcane Bagasse-Activated Carbon*

The sugarcane bagasse (SB) was obtained from a sugar factory in Ratchaburi, Thailand. Prior to the experiment, the raw material surface was cleaned using deionized water in order to remove particles of dirt, and then it was oven dried at 105 °C for 24 h. The dried SB was then cut into 3 cm pieces. The dried SB sample was carbonized under $N_2$ with an initial gas flow of 100 $cm^3$ $min^{-1}$. The carbonization was carried out for 1 h after the temperature reached 500 °C. After that, the sample was cooled down to room

temperature via $N_2$ gas flow (100 $cm^3$ $min^{-1}$). To produce AC, the carbonized SB were heated at several different temperatures, namely, 800 °C (AC800), 850 °C (AC850), 900 °C (AC900), and 950 °C (AC950), under $N_2$ gas. When the temperature rose as desired, $CO_2$ gas (100 $cm^3$ $min^{-1}$) was then introduced to activate the sample and held for 2 h each. After activation, the samples were cooled down to room temperature under $N_2$ gas at the same flow rate. The AC samples were ground and sieved at 250 and 10 µm size for Pb(II) adsorption and electrode preparation, respectively.

### *2.2. Characterization of ACs*

The physical structure and chemical properties of the AC were determined by several methods of analysis. The surface morphology of the AC samples was characterized using an FEI Quanta 450 scanning electron microscope (SEM). The samples were dried at 105 °C for 4 h and gold-sputtered for charge dissipation.

Nitrogen adsorption–desorption isotherms were measured on a Micromeritics 3 Flex surface characterization analyzer. Before the adsorption–desorption measurements, the samples were outgassed at 673 K for 8 h under a high vacuum. The BET surface area ($S_{BET}$) was calculated using the BET equation from the nitrogen sorption isotherms at 77 K. The micropore volume ($V_{mic}$) was determined using t–plot method. The pore size distribution was determined using the Barret–Joyner–Halenda (BJH) model.

Chemical characterizations were measured by fourier-transform infrared (FTIR) spectroscopy analyses so that a functional group on the surface of the samples could be identified. The FTIR analyses were prepared by mixing the samples with KBr powder and pressing to obtain a transparent pellet. The FTIR spectra were recorded using a Brucker Tensor 27 spectrometer between 4000 to 400 $cm^{-1}$.

The concentrations of carbon, hydrogen, nitrogen, and oxygen from the AC samples were identified by elemental analysis using microanalytic devices. A LECO analyzer (model CHN682 series) was used with a sample decomposition temperature of 950–1200 °C. A 1 mg sample of AC was burned, and the released gases were measured. Gaseous combustion products were calculated using a thermal conductivity detector. The difference between the total percentage and the sum of percentages of carbon, hydrogen, and nitrogen was quantified to identify the oxygen content in the sample.

### *2.3. Adsorption Studies*

A standard stock solution of 1000 mg $L^{-1}$ of Pb(II) was carried out by dissolving analytical grade reagent of lead(II) acetate ($(CH_3COO)_2$ $Pb{\cdot}3H_2O$) in deionized water using a 1000 mL volumetric flask. Batch experiments of adsorption were performed using 250 mL Erlenmeyer flasks. A volume of 50 mL of Pb(II) solution with different initial concentrations (100, 150, and 200 mg $L^{-1}$) was placed in a flask. The initial pH value of the solutions, without pH adjustment, was 5.0 pH, which was used for the equilibrium, kinetics, and adsorption studies. Following this, 0.1 g of the powdered AC was added to the Pb(II) solution. Flasks were agitated on the incubator shaker at a constant speed of 180 rpm at a room temperature of 25 °C for identified time intervals. The batch adsorption studies were conducted to ascertain the maximum adsorption capacity, optimum experimental conditions, and kinetics of the AC. Finally, the suspension was separated by filtration. Pb(II) removal by the adsorbents was determined by measuring the concentration of Pb(II) in the filtrate by atomic absorption spectroscopy using Perkin Elmer Analyst 800 atomic absorption spectrometer (AAS).

The uptake of Pb(II) ions in the solution was determined by differences in their initial and final concentrations. The data obtained were then used to calculate the equilibrium metal uptake capacity according to Equation (1):

$$q_e = \frac{V(C_0 - C_e)}{m} \quad (1)$$

where $q_e$ (mg $g^{-1}$) is the equilibrium amount of metal in the adsorbed phase, $C_0$ and $C_e$ are initial and equilibrium concentrations of metal ion (mg $L^{-1}$) in the aqueous solution, V is the volume of the solution (L), and m is the adsorbent dose (g). The adsorption isotherm experiments were performed using different concentrations of Pb(II) (100–200 mg $L^{-1}$) at room temperature. The removal percent of Pb(II) ions (% Removal) in solution was calculated using Equation (2):

$$\% \text{ Removal} = \frac{C_0 - C_e}{C_0} \times 100 \quad (2)$$

The experimental data were fitted to the adsorption isotherm and kinetic models. Analysis of adsorption models were used to provide data about the adsorption mechanism of the sample. The adsorption process was summarized under several experimental conditions, including adsorbent dose, concentration of Pb(II), volume of solution, pH, contact time, temperature, and constant speed (Table 1).

**Table 1.** The experimental conditions for adsorption study.

| Adsorption Study | Adsorbent Dose (g) | Concentration of Pb(II) (mg $L^{-1}$) | Volume of Solution (mL) | pH | Contact Time (min) | Temperature (°C) | Constant Speed (rpm) |
|---|---|---|---|---|---|---|---|
| Effect of initial pH | 0.1 | 200 | 50 | 2–6 | 180 | 25 | 180 |
| Effect of contact time | 0.1 | 200 | 50 | 5 | 15–180 | 25 | 180 |
| Adsorption isotherms and adsorption kinetics | 0.1 | 100, 150, and 200 | 50 | 5 | 15–180 | 25 | 180 |

### *2.4. Preparation of Supercapacitor Electrodes and SLP Device Assembly*

For the preparation of supercapacitor electrodes, an ink was prepared through the disperser mixing (Primix, Japan) of AC850 active material, carbon black conductive additive (C65T, Imerys), carboxymethyl cellulose (CMC) binder (MAC 300, Nippon Chemicals), and styrene butadiene rubber (SBR) binder (JSR corporation) in deionized water at a ratio of 89:5:2:4. Supercapacitor electrodes were then prepared through the application of ink to battery-grade aluminum foil via draw-down coater and a micrometer doctor blade (wet thickness ca. 150 μm), subsequent drying under vacuum at 120 °C for 12 h, and calendaring at 80 °C. The electrodes produced had a mass loading of 57–60 g $m^{-2}$ (5.7–6.0 g $cm^{-2}$).

SLP supercapacitor devices were assembled in a symmetrical arrangement with the same electrode used for both positive and negative. The electrodes were stamped to 7 × 5 cm with a 1 $cm^2$ uncoated flag area for the attachment of tabs. The electrodes were stacked with a cellulose-based separator (NKK, Japan) with one final outer wind. Aluminum tabs were then ultrasonically welded to the uncoated areas and three sides of polymer-coated, laminated aluminum pouch material were then sealed around the electrode stack. The assembled dry cell was then further dried in a glove box antechamber under dynamic vacuum at 80 °C for 72 h before being introduced into an argon-filled glove box (both $H_2O$ and $O_2$ < 0.1 ppm). The dry cells were then filled with 1.0 g electrolyte (tetraethylammonium tetrafluoroborate ($TEABF_4$, 1 M in acetonitrile (AN)), with sealing of the final edge under vacuum. The cells were stored at 25 °C for 24 h to allow for complete wetting of electrodes by electrolyte before undergoing electrochemical testing. The fully wetted cells were then conditioned electrochemically through galvanostatic cycling between 1.425 V and 2.85 V ($V_{max}$ and $V_{max/2}$), followed by a holding at 2.85 V. AC850 active material was chosen for SLP supercapacitor assembly due to it exhibiting the highest specific surface area of the AC materials produced and a high micropore pore volume. The binders, conductive additive, and current collector material in electrode preparation, along with separator and electrolyte system, were chosen to provide best possible match to those known to be used in commercial supercapacitor devices. A typical dry SLP used in this work, along with the internal assembly, is shown in Figure 1.

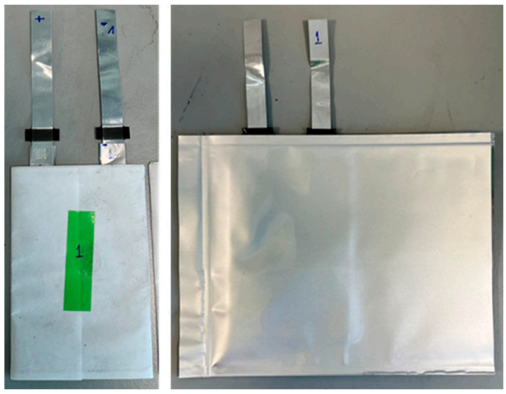

**Figure 1.** Photograph of an assembled single-layer pouch cell.

### *2.5. Electrochemical Measurements*

All electrochemical analysis was performed as 2 electrode measurements on AC850-based SLPs at 25 °C in climatic chambers. Before testing, cells were conditioned via brief galvanostatic cycling followed by a period of holding at 2.85 V. Cyclic voltammetry was performed using a Biologic VMP3 electrochemical workstation, with 5 A boosters to enable a high scan rate on pouch cell devices. The potential range studied was 0 to 2.85 V at scan rates between 5 and 1000 mV $s^{-1}$. The cell capacitance was calculated using Equation (3) and normalized by mass to provide the specific capacitance:

$$C = \frac{1}{2\upsilon m}\int I \cdot dV \tag{3}$$

where $C_{sp}$ is the specific capacitance (F $g^{-1}$), $\upsilon$ is the scan rate (mV $s^{-1}$), m is the active material mass, I is current (A), and V is potential (V).

Galvanostatic charge–discharge cycling was performed using a Maccor 4000 battery tester. The cells were cycled between 1.425 and 2.85 V ($V_{max/2}$ and $V_{max}$) to assess capacitance and ESR (1 s), with capacitance calculated using Equation (4) and ESR calculated from the voltage change at end of discharge to 1 s rest using Equation (5):

$$C_{sp} = \frac{4I \times t}{\Delta V \times m} \tag{4}$$

where $C_{sp}$ is the specific capacitance (F $g^{-1}$), I is the current (A), t is time (s), $\Delta V$ is the potential difference, and m is the mass of active material (g) in both electrodes.

$$ESR = \frac{I}{\Delta V} \tag{5}$$

where ESR (W) is the equivalent series resistance, I (A) is the discharge current, and $\Delta V$ (V) is the difference in potential between the end of discharge and 1 s rest.

Rate performance was assessed with varied discharge current densities of 1, 2.5, 5.0, 7.5, and 10.0 A $g^{-1}$ with cycle lifetime assessed through GCD cycling at 1.0 A $g^{-1}$ over 10,000 cycles. The energy–power density relationship was assessed through constant power cycling at fixed powers between 50 and 2500 W $Kg^{-1}$ (or 1000 in the case of total pouch mass), as directed through USABC FreedomCar [49], with the energy calculated through Equation (6) and normalized to mass (of active material or cell). Constant power cycling was performed using two masses (i.e., two sets of cycling at two sets of power densities) based on that of the active material and also based on the total mass of the packaged SLP.

$$E = \int IV \cdot dt \tag{6}$$

where E is the energy density (Wh), I is current (A), and V is potential (V).

## 3. Results and Discussion

### *3.1. Activated Carbon Yield*

The yield in the production of activated carbon is typically calculated as the mass of the final activated carbon produced after activation divided by the mass of the precursor. The activated carbon yield was calculated using Equation (7):

$$\text{Yield } (\%) = \frac{m_{AC}}{m_P} \times 100 \quad (7)$$

where $m_{AC}$ is the mass of activated carbon (g) and $m_P$ is the mass of precursor (g).

The percentage yield of activated carbon as represented in Table 2. Based on the data as shown in Table 2, the percentage of yield decreases from 55.30 to 39.79 %. The findings indicated that the percentage yield was influenced by the activation temperature. The oxygen-containing groups were decreased with increase of the activation temperature. This is because at high activation temperature, ash, volatile matter, and moisture content were removed from carbon's porous structure and generated residue ash.

**Table 2.** The percentage yield of activated carbon.

| Sample | Activation Temperature (°C) | Yield (%) |
|---|---|---|
| AC800 | 800 | 55.30 |
| AC850 | 850 | 53.95 |
| AC900 | 900 | 46.25 |
| AC950 | 950 | 39.79 |

### *3.2. Scanning Electron Microscopy*

The SEM technique was used to produce a micrograph to investigate the surface of AC. The SEM micrographs are illustrated in Figure 2. The SEM micrographics were recorded with a sample coating by gold for charge dissipation with 50,000× magnification. As a reaction to the decomposition that occurred during activation processes, which produced and released the biochar's remaining volatile matter, the remaining nonvolatile components were changed into AC with pores of various shapes and sizes, as shown on the surface [50]. The figure illustrates that the samples had an irregular and porous surface, indicating that the AC has a relatively high surface area. The AC800 sample had a compact irregular structure with flake-shaped particles, while AC950 has more crater-like pores produced during the release of reaction gases from the core toward the outer surface as a result of the higher activation temperature. It can be observed from the SEM image that the external surface has cracks of various sizes, making some large holes. This observation is supported by the BET surface area of the samples.

### *3.3. Surface Area and Pore Size Distribution*

The nitrogen adsorption–desorption isotherms and pore size distribution curves of ACs are presented in Figure 3a. The isotherms of samples show the typical hysteresis loop corresponding to a Type IV isotherm according to the IUPAC classification indicating the mesoporous character of the carbon material. Type IV isotherms occur when capillary condensation ($P/P_0 > 0.45$) occurs. The BET surface area of mesoporous structures, which are samples with pore diameters between 2–50 nm, produces this type of isotherm [51]. The trends of the isotherms are quite similar. In physical activation, the final activation temperature is an important parameter in producing the surface area and the pore volume of the AC. The activation temperature has effects on the surface area ($S_{BET}$) and pore volume (total, micropore, and mesopore) of the AC, which are summarized in Table 3. The results illustrate that as the activation temperature rose from 800 to 900 °C, this resulted in the $S_{BET}$ and $V_{tot}$ values increasing significantly. The BET surface area of AC950 decreased, showing that the increasing mesopore volume and decreasing micropore volume can affect the surface area. Therefore, the increasing activation temperatures trend was reversed as a

result of the carbonization effect of the volatiles and the retraction of AC structure, which resulted in the contraction of some of the pores.

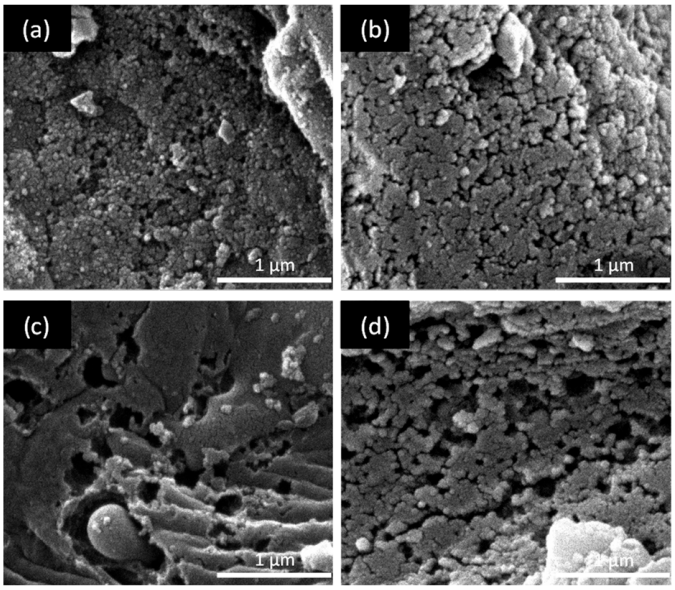


**Figure 2.** SEM micrographs of AC800 (**a**), AC850 (**b**), AC900 (**c**), and AC950 (**d**).

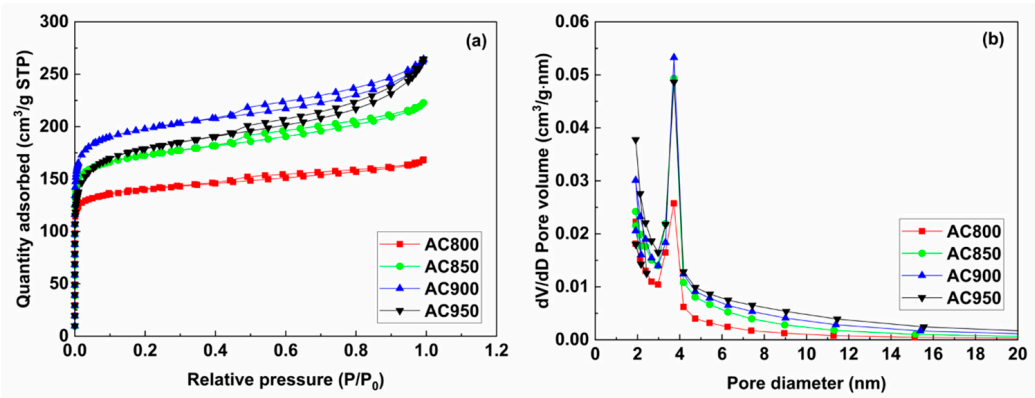


**Figure 3.** Nitrogen adsorption–desorption isotherm (**a**) and pore size distribution curves (**b**) of the activated carbon samples.

**Table 3.** Specific surface areas and pore volumes of activated carbons.

| Sample | $S_{BET}$ ($m^2$ $g^{-1}$) | $V_{tot}$ ($cm^3$ $g^{-1}$) | $V_{mic}$ ($cm^3$ $g^{-1}$) | $V_{mes}$ ($cm^3$ $g^{-1}$) | D (nm) |
|---|---|---|---|---|---|
| AC800 | 509.43 | 0.540 | 0.143 | 0.396 | 4.24 |
| AC850 | 766.52 | 0.782 | 0.179 | 0.603 | 4.66 |
| AC900 | 671.29 | 0.991 | 0.188 | 0.804 | 5.17 |
| AC950 | 673.79 | 0.918 | 0.118 | 0.800 | 5.45 |

$S_{BET}$: BET surface area; $V_{tot}$: total pore volume; $V_{mic}$: micropore volume; $V_{mes}$: mesopore volume; D: average pore diameter.

The pore size distribution curves of the AC samples are illustrated in Figure 3b. The results clearly demonstrate that the AC samples have a largely mesoporous structure. The average pore diameter of samples increased from 4.24 nm to 5.45 nm (Table 3) with an increasing activation temperature.

### *3.4. Fourier-Transform Infrared Spectroscopy*

The FTIR spectrum of AC with different activation temperatures is shown in Figure 4. The FTIR spectra show numerous adsorption peaks, demonstrating the complex nature

of the samples. Irrespective of the different activation temperatures provided, it can be observed that the overall shapes of the spectra are quite similar. The broad absorption band of 3600–3200 $cm^{-1}$ with a peak around 3444 $cm^{-1}$ is ascribed to the O–H stretching vibration of hydrogen-bonded hydroxyl groups [23]. The appearance of the band around 2922 $cm^{-1}$ can be ascribed to the asymmetric vibration of C–H groups [10]. The adsorption band at 1558 $cm^{-1}$ is ascribed to C=C stretching vibration in the aromatic ring [52]. The peaks observed around 1300–1000 $cm^{-1}$ correspond to the C–O stretching vibration of carboxylic acids and alcohols [53]. Peaks at a low wavenumber around 794 $cm^{-1}$ may be related to the plane-bending vibrations mode of C–H groups [54]. Additionally, the FTIR analyses showed that the surface functional groups of AC obtained at different activation temperatures were similar and possibly formed due to the oxidative degradation from heat treatment stages.

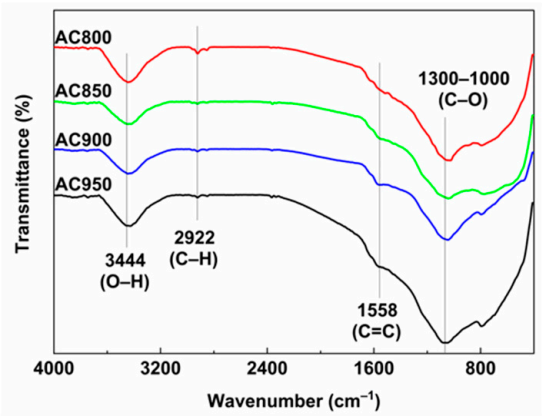


**Figure 4.** FTIR spectra of the activated carbon samples.

### *3.5. Elemental Analysis*

Elemental analysis of the adsorbents is shown in Table 4. The content of the elements changed when the temperature of activation was increased. The results demonstrate that the activation temperature leads to a decrease in carbon content. At the same time, there is an increase in the quantity of oxygen content with increasing activation temperature. Small amounts of hydrogen and nitrogen have also been detected. The content of nitrogen showed some fluctuations.

**Table 4.** Elemental analysis data of the samples.

| **Elemental Analysis (wt.)** | | | | |
|---|---|---|---|---|
| **Sample** | **C** | **H** | **N** | **O** [a] |
| AC800 | 58.89 | 1.69 | 0.50 | 38.92 |
| AC850 | 73.50 | 1.74 | 0.51 | 24.25 |
| AC900 | 57.36 | 1.30 | 0.56 | 40.78 |
| AC950 | 39.59 | 1.22 | 0.43 | 58.79 |

[a] Calculated by difference.

### *3.6. Effect of Initial pH Value*

Both the surface properties of the adsorbent and the pH of the aqueous solution are important factors in adsorption studies. The pH is important because it can affect the extent of adsorption and the number of metal ions formed in the solution [55]. The adsorption performance of Pb(II) on the AC surface has been examined over a pH range of 2.0–6.0 at room temperature. Figure 5 shows the influence of the initial pH solution on the removal of Pb(II) by AC; the initial concentration of Pb(II) solution was 200 mg $L^{-1}$ at a contact time of 180 min. The Pb(II) removal by AC increased with increasing pH, up to a maximum of 59.15% at an initial pH of 5.0. Below and above these pHs, the adsorption

level decreased. Above pH 6.0, precipitation of oxides of Pb(II) was formed; therefore, the study was confined to a pH range of 2–6.

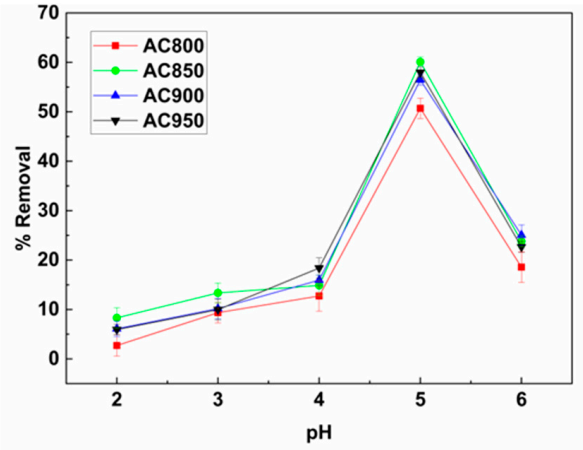


**Figure 5.** The effect of initial pH value on the adsorption of Pb(II) ions onto the activated carbon samples. (Condition: 50 mL of Pb(II) at initial concentration 200 mg $L^{-1}$, contact time: 180 min, constant speed: 180 rpm, and adsorbent dose: 0.1 g.)

### *3.7. Effect of Contact Time*

The effect of contact time on the AC to Pb(II) concentration on adsorption capacity was observed across the ranges of 15–180 min. Figure 6 shows the effect of contact time at an initial concentration of Pb(II) solution is 200 mg $L^{-1}$ at room temperature. The agitation was held at a constant speed of 180 rpm throughout the experiments. It can be observed that the removal percent of Pb(II) ions by all AC increased sharply with the contact time until the equilibrium was attained. The equilibrium times for AC were 120 min. At 180 min, the percentage removal of Pb(II) ions was 57.82% from AC850 at the highest specific surface area. The high percentage removal of Pb(II) on the activated carbon confirms that the adsorption process is related to the BET surface area, total pore volume, and average pore size. This equilibrium time result is of interest because time efficiency is one of the parameters that wastewater treatment plant applications need to focus on.

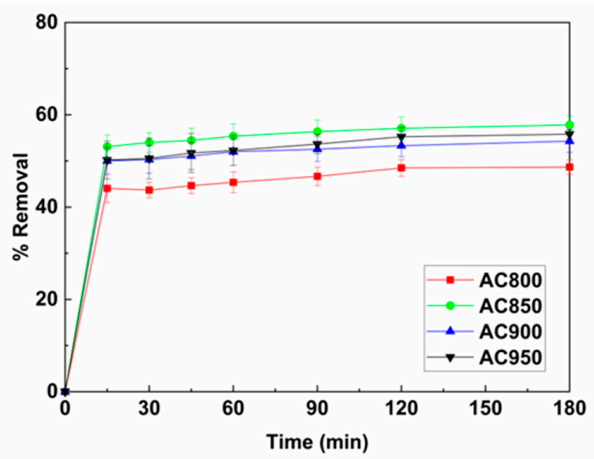


**Figure 6.** The effect of contact time on the adsorption of Pb(II) ions onto the activated carbon samples. (Condition: 50 mL of Pb(II) at initial concentration 200 mg $L^{-1}$, pH 5.0, constant speed: 180 rpm, and adsorbent dose: 0.1 g.)

### *3.8. Adsorption Isotherm Models*

To describe the adsorption process and examine the mechanisms of adsorption of Pb(II) on the AC. The Langmuir, Freundlich, Temkin, Dubinin–Radushkevich, Toth, Koble–Corrigan, and Redlich–Peterson isotherms are the most frequently utilized in liquid/solid

systems. The two most used isotherms for treating wastewater are the Langmuir and Freundlich isotherm models [56,57]. The adsorption equilibrium data corresponds to the correlation between the mass of the Pb(II) ions adsorbed per unit mass of AC ($q_e$) and the concentration of Pb(II) solution at equilibrium ($C_e$) [58].

The Langmuir adsorption isotherm is frequently used to describe the equilibrium adsorption process. This model can be used in the linear of Langmuir Equation (8):

$$\frac{C_e}{q_e} = \frac{1}{K_L q_m} + \frac{C_e}{q_m} \tag{8}$$

where $q_e$ is the equilibrium adsorption amount that can be adsorbed (mg $g^{-1}$), $q_m$ is the saturated adsorption amount (mg $g^{-1}$), $K_L$ is the Langmuir isotherm adsorption rate constant associated with the adsorption rate (L $mg^{-1}$), and $C_e$ is the equilibrium concentration of the solution (mg $L^{-1}$).

The experimental data can be represented via this linear form of the equation by plotting $C_e$ versus $C_e/q_e$, as shown in Figure 7. Based on the intercept and slope of the plot, the Langmuir constants $K_L$ and $q_m$ can be evaluated, respectively.

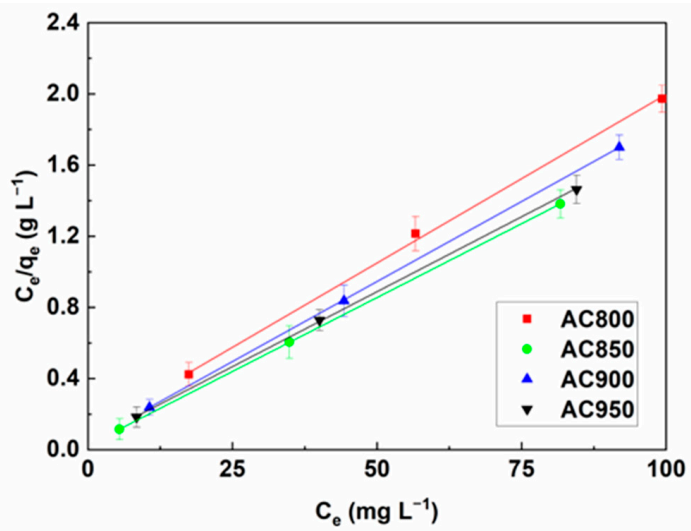


**Figure 7.** Langmuir adsorption isotherms of Pb(II) ions onto the activated carbons.

The Freundlich isotherm can be represented as adsorption behavior on an uneven surface. This model can be written in the linear form, as follows in Equation (9):

$$\log(q_e) = \log(K_F) + \frac{1}{n}\log(C_e) \tag{9}$$

where $K_F$ is the capacity factor, which indicates solid adsorbent capacity at a specific concentration of a solution (mg $g^{-1}$) and n is the constant that depends on several environmental factors and describes a nonlinear degree of adsorption isotherm.

A line can be determined by plotting $\log(C_e)$ versus $\log(q_e)$. If the data fit well with the Freundlich isotherm model, the constants can be obtained from the intercept and the slope, as shown in Figure 8. Both of the parameters $K_F$ and 1/n affect the adsorption isotherm. The larger the $K_F$ and 1/n value, the higher the adsorption capacity [59].

In this work, the Langmuir and Freundlich models were utilized to describe the relationship between the amount of adsorption Pb(II) ions and their equilibrium concentration in an aqueous solution at room temperature for 180 min. The adsorption isotherm was determined at a concentration range of 100–200 mg $L^{-1}$. In all experiments, 0.1 g of adsorbent was used with a volume of 50 mL of Pb(II) solution at pH 5.

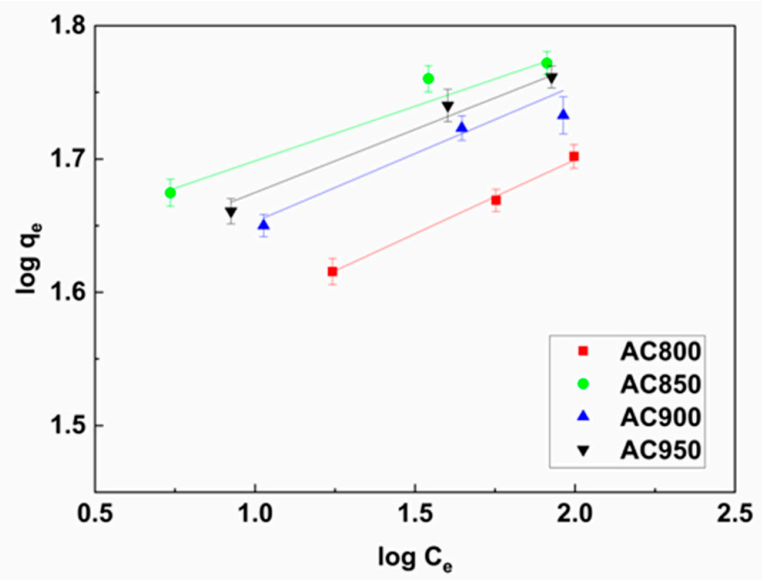


**Figure 8.** Freundlich adsorption isotherms of Pb(II) ions onto the activated carbons.

The parameters of adsorption isotherms of AC are summarized in Table 5. These isotherms fit with the Langmuir model with correlation coefficients ($R^2$) all > 0.99. $R^2$ is used as a measure of the goodness of fit; the closer $R^2$ approaches 1, the better the fit. The maximum adsorption capacities ($q_m$) calculated by Langmuir isotherm were 52.91 mg $g^{-1}$ (AC800), 60.24 mg $g^{-1}$ (AC850), 55.56 mg $g^{-1}$ (AC900), and 59.52 mg $g^{-1}$ (AC950). The results showed that when the activation temperature increased, the $K_L$ values decreased, indicating that the amount of Pb(II) adsorption on AC reduced with the activation temperature increasing. The results according to $q_m$ values obtained using the Langmuir isotherm model indicate that the Pb(II) adsorption capacity of AC decreased when activation temperature increased beyond 850 °C.

**Table 5.** Adsorption isotherm model parameters for Pb(II) adsorption.

| Sample | Langmuir | | | Freundlich | | |
|---|---|---|---|---|---|---|
| | $q_m$ (mg $g^{-1}$) | $K_L$ (L $mg^{-1}$) | $R^2$ | $K_F$ (mg $g^{-1}$) | n | $R^2$ |
| AC800 | 52.91 | 0.1720 | 0.9987 | 29.81 | 8.86 | 0.9956 |
| AC850 | 60.24 | 0.6510 | 0.9998 | 41.20 | 11.56 | 0.9592 |
| AC900 | 55.56 | 0.4063 | 0.9989 | 36.25 | 10.82 | 0.9465 |
| AC950 | 54.52 | 0.3552 | 0.9999 | 36.97 | 9.71 | 0.9857 |

For the Freundlich isotherm, the $K_F$ values are associated with the capacity of the Pb(II) adsorption on the adsorbent. In the results, the $K_F$ values decreased after 850 °C of activation temperature. The n values in Freundlich isotherm are a function of the strength of adsorption. The higher n values indicate higher adsorption capacity.

### *3.9. Adsorption Kinetics*

The adsorption kinetics data of Pb(II) was analyzed by fitting the data with the following pseudo-first order and pseudo-second order rate equations. The pseudo-first order equation is the most commonly used for the adsorption rate from aqueous solution and is generally expressed as Equation (10):

$$\frac{\log(q_e - q_t)}{q_e} = -\frac{k_1 t}{2.303} \quad (10)$$

The pseudo-second order kinetic model is based on equilibrium adsorption. It can be represented in the following from Equation (11):

$$\frac{t}{q_t} = \frac{1}{(k_2 q_e^2)} + \frac{t}{q_e} \tag{11}$$

where $k_1$ is the pseudo-first order rate constant of adsorption ($min^{-1}$), $q_t$ is the adsorption capacity at a given time (mg $g^{-1}$), $q_e$ is the adsorption capacity at equilibrium (mg $g^{-1}$), t is the time (min), and $k_2$ is the pseudo-second order adsorption rate constants (g mg·$min^{-1}$).

The constants in the above equations ($k_1$ and $k_2$) can be observed from the slopes of linear plots of $\log(q_e - q_t)$ versus t and $t/q_t$ versus t, whereas $q_e$ can be obtained from the intercept data for the pseudo-second order and second order rate equations.

It is necessary to analyze adsorption kinetics in order to provide data about the adsorption mechanism of AC. All kinetic data results of Pb(II) adsorption onto AC that are calculated from the equations are summarized in Table 6. According to the results, the pseudo-second order model illustrated fits better for all AC samples than the pseudo-first order model. The $q_e$ values of the pseudo-second order model are closer to the $q_e$ values of the experiment, with higher $R^2$ values ($R^2 > 0.99$).

**Table 6.** Kinetic model parameters for Pb(II) adsorption.

| Sample | $q_{e,\ exp}$ | Pseudo–First Order | | | Pseudo–Second Order | | |
|---|---|---|---|---|---|---|---|
| | | $q_{e,\ cal}$ | $k_1$ | $R^2$ | $q_{e,\ cal}$ | $k_2$ | $R^2$ |
| AC800 | 50.35 | 4.35 | 0.0111 | 0.7992 | 48.78 | 0.0316 | 0.9995 |
| AC850 | 59.15 | 8.77 | 0.0415 | 0.9250 | 59.17 | 0.0212 | 0.9997 |
| AC900 | 54.05 | 5.79 | 0.0193 | 0.9399 | 53.19 | 0.0210 | 0.9995 |
| AC950 | 57.75 | 10.11 | 0.0134 | 0.9487 | 54.95 | 0.0122 | 0.9985 |

Numerous studies have been undertaken which use various types of adsorbents to adsorb Pb(II) ions. The Pb(II) adsorption capacities of this present study were compared with other adsorbents using the Langmuir isotherm and are presented in Table 7. The findings of this study were consistent with findings of earlier studies, which found that the adsorption process resembled pseudo-second order kinetics. Adsorption kinetics plays a key role in explaining the rate of reaction and mechanisms that lead to adsorption.

**Table 7.** Adsorption capacities of different adsorbents for Pb(II) ions.

| Absorbent | Activation Method | Activating Agent | Adsorption Condition | | | Ref |
|---|---|---|---|---|---|---|
| | | | pH | Adsorbent Dose (g $L^{-1}$) | $q_m$ (mg $g^{-1}$) | |
| Olive branches | Chemical activation | $H_3PO_4$ | 5.0 | 20.0 | 41.32 | [60] |
| Kesambi wood | Chemical activation | $H_2SO_4$ | 5.0 | 8.0 | 1.63 | [61] |
| Cumin seeds | Chemical activation | $H_2SO_4$ | 4.8 | 5.0 | 17.98 | [62] |
| Sugarcane bagasse | Physical activation | $CO_2$ | 5.0 | 2.0 | 60.24 | This study |

### *3.10. Electrochemical Properties*

The electrochemical properties of AC850 have been investigated through cyclic voltammetry between 0 and 2.85 V at scan rates from 5 to 1000 mV $s^{-1}$, as shown in Figure 9.

The cyclic voltammograms were as expected for a carbon-based organic electrolyte supercapacitor, displaying a rectangular form that is typical EDLC capacitive behavior. A broad possible peak can be seen at low scan rates centered at 1.5 V in the cathodic direction and is ascribed to the reduction of oxygen functionality on the carbon surface, as discussed below in relation to GCD results. As the scan rate was increased to 100 mV $s^{-1}$ and above, a distortion in the rectangular nature of the CVs was observed, along with tilting away from the horizontal, becoming significant at 500 mV $s^{-1}$ and above. This deviation from the

horizontal rectangular CV is a result of limitations in accessibility of ions to and from the electrode surface in the pore structure at the rates under observation [63,64]. At the lower scan rates, there is sufficient time for ions to migrate to the electrode surface throughout the electrode and effectively store charge through double-layer formation. As the rate increases, a reduced amount of double-layer formation is observed due to ions not being able to access the full pore structure of the electrode.

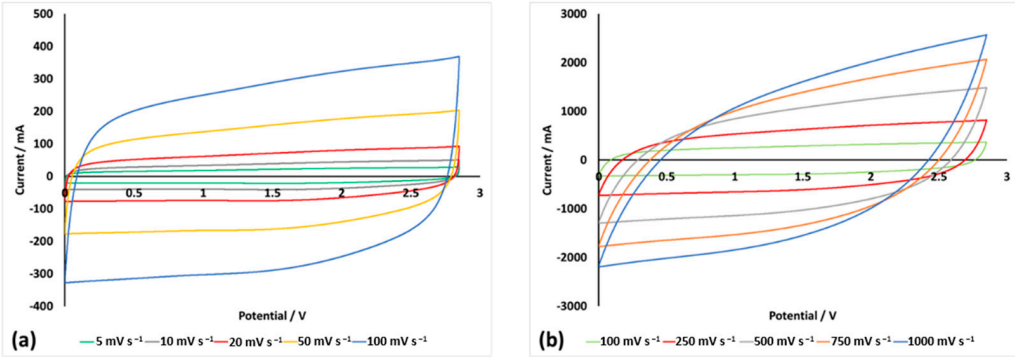


**Figure 9.** CV profiles of AC850 SLPs at various scan rates (**a**) between 5 and 100 mV $s^{-1}$ and (**b**) between 100 and 1000 mV $s^{-1}$.

This is further observed through the rate data, as shown in Figure 10. The scan rates (and hence discharge rates) in this work represent a significant range of operation times for such an energy storage device, with the range of 5 to 1000 mV $s^{-1}$ corresponding to a discharge time of 570 to 2.85 s (assuming a discharge to 0 V). The specific capacitance is seen to decrease from ca. 42 to 25 F $g^{-1}$ as the scan rate increases from 5 to 200 mV $s^{-1}$, with the relative decrease in rate being less significant as the rate is increased further to 1000 mV $s^{-1}$.

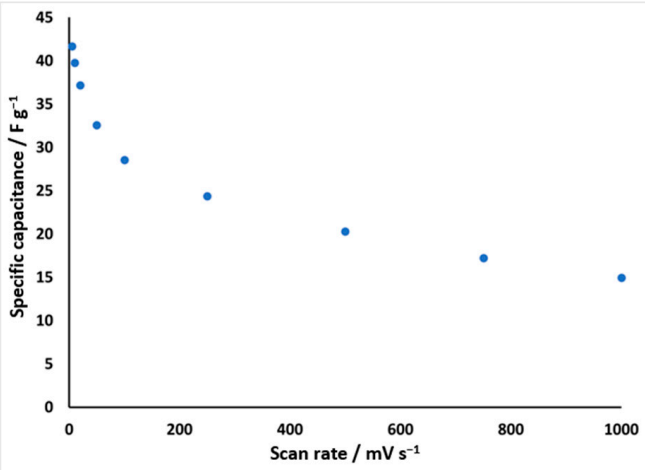


**Figure 10.** Rate performance through variation in specific capacitance of AC850 SLPs as determined through CV.

The capacitance, ESR, and lifetime characteristics of AC850 SLP cells have been investigated through GCD between 1.425 and 2.85 V corresponding to $V_{max}$ and $V_{max/2}$. This potential range is chosen (rather than 0 to 2.85 V) as it aligns with testing typically performed at device and commercial cell level and that suggested through USABC FreedomCar [49] testing criteria. A specific capacitance and ESR of 27 F $g^{-1}$ and 0.25 Ω, respectively, were observed from GCD at a current density of 1 A $g^{-1}$. Whilst the ESR was typical for a device of this size and engineering, the specific capacitance was lower than first expected for activated carbon in such a system. With this in mind, it is timely to note that the materials used in this work were optimized for Pb(II) adsorption as described, with the assumption

that this is not the optimized form for supercapacitor application; this work aimed to provide an indicator for potential application and an assumption of the improvement of properties for this family of materials through further processing (e.g., tailoring of pore size distribution, pore volume and surface area, further thermal treatment for removal of functional groups, etc.). Factors effecting the specific capacitance can be seen from the characterization data already reported in this work, with particular attention drawn to the high proportion of mesoporosity and high pore volume for this material, with this expected to limit the gravimetric-specific capacitance in comparison to a more microporous material. In addition, the elemental analysis of the material showed a high amount of oxygen present, with the FTIR indicating the presence of oxygen-containing functional groups. It is known that the presence of surface oxygen functionality on carbons has a detrimental effect on both the capacitance and lifetime of organic electrolyte supercapacitors [65,66]. This reduction in capacitance is a result of a blocking of sites for ion adsorption, a reduction in carbon electronic conductivity, and degradation of the surface through various decomposition mechanisms during operation [65,66]. As detailed in the Materials and Methods Section, the SLPs were conditioned prior to testing through brief cycling and held at 2.85 V. This 2.85 V hold, in addition to ensuring wetting and access of deepest pore structure, represents the most aggressive of conditions for degradation of oxygen-containing (and other) functional groups, with their degradation further impacting the capacitance of the material through degradation of the surface of the carbon and the blocking of some pore structure and electrode access for ions through the deposition and growth of degradation products. The specific capacitance observed prior to conditioning was ca. 40 F $g^{-1}$, suggesting a loss of 32% of specific capacitance through this process, assumed to be in large part a result of the identified oxygen functionalization. It is anticipated that the specific capacitance observed in AC850 could be greatly enhanced through post-synthesis heat treatment to remove functionalization under an argon atmosphere and through tailoring of the pore structure during synthesis. For reference, a typical specific capacitance for a bioderived AC with high surface-specific surface area (>2000 $m^2$ $g^{-1}$) and tailored porosity and surface functionality would be ca 90 F $g^{-1}$ [67]. The charge–discharge profile observed during GCD at current densities between 1 and 10 A $g^{-1}$ is shown in Figure 11.

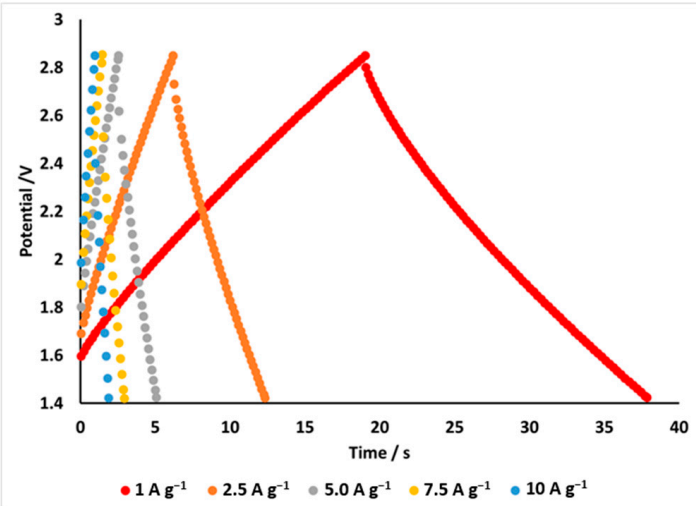


**Figure 11.** GCD charge–discharge profiles of AC850 SLPs at current densities between 1 and 10 A $g^{-1}$.

The typical symmetrical sawtooth profile is observed in all cases with a slight deviation being seen at the lower current densities at higher potential. This minor deviation is believed to be a result of faradaic and or parasitic/degradation processes occurring due to the previously mentioned functionalization and possible impurities in the carbon. During continued cycling, this deviation is seen to decrease and the profile move towards the ideal sawtooth. The ohmic "ir drop" corresponding to cell ESR can be seen between the end of

charge and the start of discharge, with ESR calculated to be 0.25 Ω (as calculated at the end of discharge, as described in the Materials and Methods Section), corresponding to an area-specific resistance of 7 mΩ $cm^{-2}$.

Figure 12 shows the rate behavior as the current density is increased from 1 to 10 A $g^{-1}$, with a corresponding decrease in specific capacity from 27 to 14 F $g^{-1}$. The decrease in specific capacitance with increasing current density is again a result of the limitations in accessibility of ions to and from the electrode surface in the pore structure at the rates under observation, as described and observed in CV analysis.

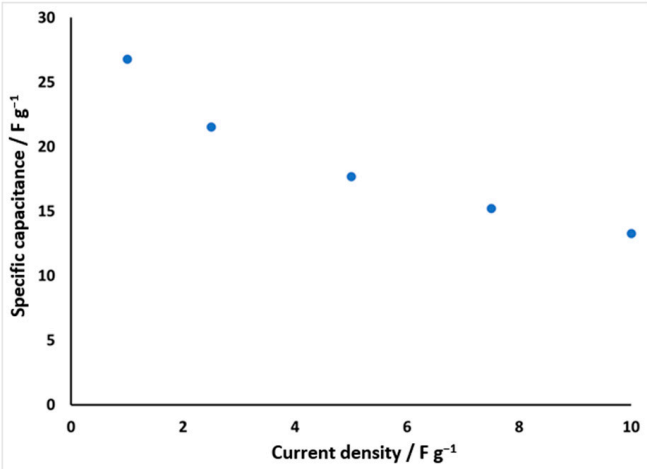


**Figure 12.** Rate performance through variation in current density of AC850 SLPs as determined through GCD.

Despite a 50% decrease in specific capacity over the range measured, this corresponds to a 10-fold increase in current density and corresponding decrease in discharge time from 37 s at 1 A $g^{-1}$ to 2 s at 10 A $g^{-1}$ and, as such, is seen as good rate performance, suggesting high power potential, as demonstrated in the constant power cycling that follows.

The specific capacitance observed through GCD can be seen to be lower than that observed through CV. This difference can be reconciled through consideration of the overall discharge rate for each step in either technique, with the discharge times and specific capacitance matching at 1000 mV $s^{-1}$ vs 7.5 A $g^{-1}$, 500 mV $s^{-1}$ vs. 5 A $g^{-1}$, and 200 mV $s^{-1}$ vs. 2.5 A $g^{-1}$. Long-term cycle life performance was investigated through GCD cycling between 1.425 and 2.85 V at a current density of 1 A $g^{-1}$ over 10,000 cycles, and is shown in Figure 13.

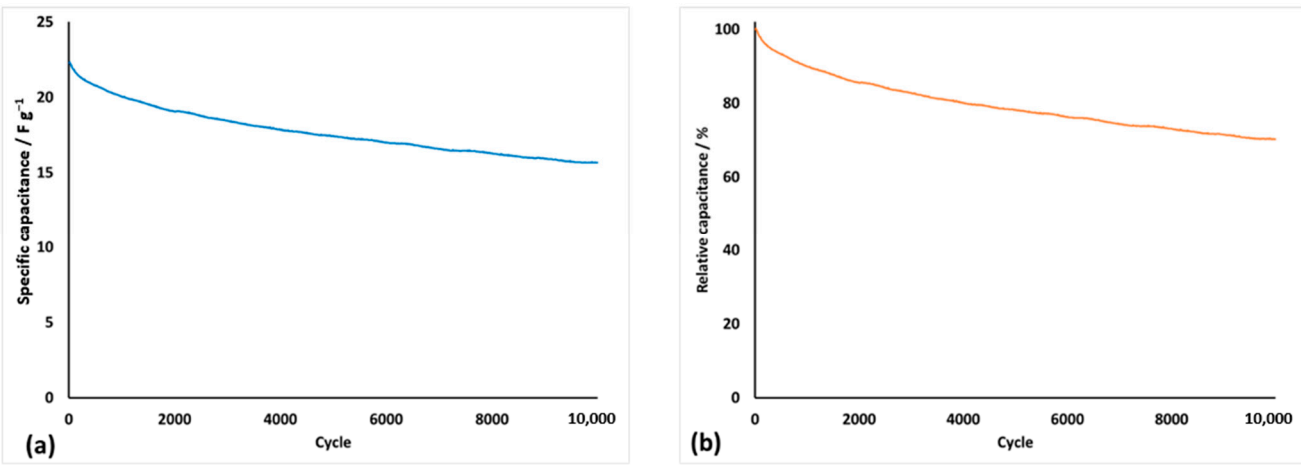


**Figure 13.** Cycle life assessment of AC850 SLPs cycled at 1 A $g^{-1}$ as expressed as (**a**) specific capacitance and (**b**) relative capacitance (relative to first cycle-specific capacitance).

The specific capacitance was seen to decrease from 22 to 16 F $g^{-1}$ over 10,000 cycles, corresponding to a retention of 70%, with the 80% retention value reached after 4000 cycles. The 80% retention of capacitance is regarded by many as the-end-of-life point for supercapacitor devices. The drop to 70% over 10,000 cycles is to be expected in this system due to the presence of high oxygen functionalization, as discussed earlier, with this providing a degradation route for both the carbon electrodes and electrolyte whilst also resulting in the blocking of surface sites and pore structure through deposition of degradation products. It is expected that the cycle life of supercapacitors from AC850 and the wider family of materials possible via the route and precursors discussed in this work would exhibit a significantly higher cycle lifetime after post-synthesis heat treatment in an inert environment to remove oxygen functional groups and improve purity.

The electrochemical impedance spectra (EIS) of SLPs were measured at 0, 1.425, 2.14, and 2.85 V. Complex impedance Nyquist plots of the same form were obtained at each potential, as shown in Figure 14. At high frequency, a depressed semicircle is observed and assigned to charge transfer processes at the electrode–electrolyte interface. The intersect with the real axis indicates the electrode resistance (Rs), including contact resistance between the electrode and current collector, tab resistance, and wires and connections, with the diameter of the following semicircle corresponding to electrolyte/charge transfer resistance. Moving to lower frequency, the 45° line transitioning to 90° at the knee frequency is indicative of capacitive behavior and of a semi-infinite Warburg component indicative of diffusive layer resistance and ion diffusion in pores, with the lowest frequency region indicating the equilibrium differential capacitance [63,68,69].

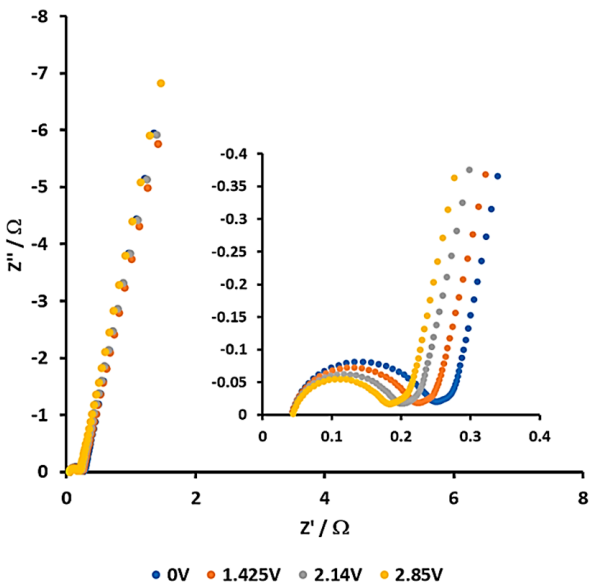


**Figure 14.** Complex impedance behavior of AC850 SLPs at different potentials.

No change was observed in Rs but the charge transfer resistance was seen to decrease as the cell potential increases, with no change observed in the diffuse layer resistance. As expected, an increase in diffuse equilibrium capacitance was observed as the potential was increased to the maximum corresponding to a fully charged device.

The energy–power relationship of the SLPs was investigated through the Ragone behavior, as seen in Figure 15. The cells were cycled at constant power to provide power densities based on the active material mass and device mass. The energy density observed through application of constant power based on active material illustrates the high power–high energy potential of the AC850 material, with an energy density of 10 Wh $Kg^{-1}$ with little loss up to a power density of 2500 W $Kg^{-1}$.

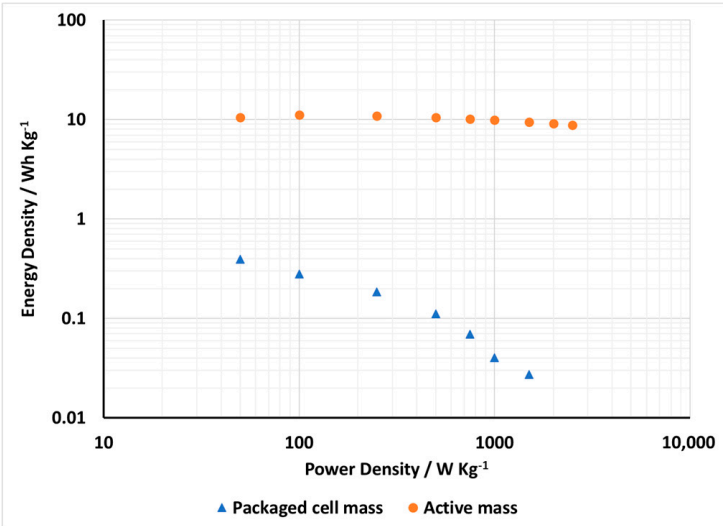


**Figure 15.** Ragone plot of energy density–power density as measured through constant power cycling based on both active material and packaged cell mass.

Whilst it is commonplace for such Ragone plots to utilize the energy and power densities as calculated from active material mass, the comparison with commercial device performance cannot be realistically made because in such devices, the packaging and all other materials are taken into account when the mass is considered. The plot energy–power plot in Figure 15 corresponding to the actual device mass (as would be the case with a full device) illustrates the large disparity present between the values obtained through the two different approaches mentioned. Through the use of the device mass in the calculation of power to be applied during testing, the current needed to be applied, relative to that for the active material mass testing, approximately 24 times. The utilization of this approach to an SLP cell is an extreme case, given the very small ratio of active material to packaging material, tabs, etc., and, as such, the energy observed is much lower than would be expected in a packaged larger cell (Commercial Maxwell 2.7V, 3000F, BCAP3000 cell, 12.3 kW $Kg^{-1}$ and 6.9 Wh $Kg^{-1}$ [70]). It does, however, serve to illustrate the need for clarity and transparency when assessing the performance of a material and comparing it to other commercial (or prototype) devices.

## 4. Conclusions

Sugarcane bagasse AC produced by physical activation using $CO_2$ was an efficient and effective adsorbent for the removal of Pb(II) from an aqueous solution. SEM and nitrogen adsorption at 77 K showed mesoporosity of ACs, the rupturing effect of activation temperature of the volatiles, and the retraction of the carbon structure. These activation processes introduce oxygen-containing functional groups onto the surface of the AC. The adsorption of Pb(II) onto AC was found to greatly depend on contact time as well as the initial concentration and pH of the aqueous solution. This study has demonstrated that the adsorption process fits well with the Langmuir isotherm model as well as the pseudo-second order kinetic model ($R^2 > 0.99$) best described the adsorption of Pb(II). The monolayer adsorption capacity ($q_m$) calculated from the Langmuir isotherm model was 60.24 mg $g^{-1}$ at an initial pH of 5.0, contact time of 180 min, and constant speed of 180 rpm achieved for AC850. The high adsorption capacity of this adsorbent indicates that sugarcane bagasse AC can effectively remove heavy metal ions from wastewater.

The electrochemical performance of AC850 was assessed to understand its potential as an active material for supercapacitor application. The materials used in this work were optimized for Pb(II) adsorption as described, with the assumption that this is not the optimized form for supercapacitor application; this work aimed to provide an indicator for potential application and an assumption of the improvement of properties for this

family of materials through further processing (e.g., tailoring of pore size distribution, pore volume and surface area, further thermal treatment for removal of functional groups, etc.). The SLP supercapacitor cells assembled using AC850 electrodes showed a specific capacitance as high as 42 F $g^{-1}$, with their rate behavior demonstrated over a wide range of current densities and scan rates corresponding to discharge from 10 min to 2 s. Reasonable cycle life has been demonstrated, with 4000 cycles achieved to a retained capacitance of 80% and 10,000 cycles to 70%. Furthermore, a high energy density was demonstrated through constant power cycling based on active mass of the material, with the Ragone characteristics also demonstrated when considering the fully packaged cell. The results for the AC850 optimized for Pb(II) sorption demonstrated the potential for both sugarcane bagasse and the synthetic route to activated carbon for potential as supercapacitor devices; however, we concluded that further modification of pore size and surface area along with a thermal post-treatment to reduce oxygen content and functionalization of the carbon surface would be most beneficial for enhanced capacitance, rate performance, and lifetime in supercapacitor application.

**Author Contributions:** Conceptualization, A.J.R. and S.T.; methodology, W.S. and A.J.R.; software, A.J.R.; validation, W.S., A.G. and A.J.R.; formal analysis, W.S., A.G. and A.J.R.; investigation, W.S., A.G. and A.J.R.; resources, A.G., A.J.R. and S.T.; data curation, W.S., A.G. and A.J.R.; writing—original draft preparation, W.S., A.G. and A.J.R.; writing—review and editing, W.S. and A.J.R.; visualization, W.S. and A.J.R.; supervision, A.J.R. and S.T. All authors have read and agreed to the published version of the manuscript.

**Funding:** This research was funded by the Royal Golden Jubilee (RGJ) Ph.D. Programme, grant number PHD/0191/2560, and funded by the Department of Physics, Faculty of Science, Kasetsart University, Thailand.

**Institutional Review Board Statement:** Not applicable.

**Informed Consent Statement:** Not applicable.

**Data Availability Statement:** The authors confirm that the data supporting the findings of this study are available within the article.

**Acknowledgments:** The authors wish to acknowledge the financial support provided by the Royal Golden Jubilee (RGJ) Ph.D. Programme (Grant No. PHD/0191/2560) through the Thailand Research Fund (TRF). Moreover, this research has received funding support from the NSRF via the Program Management Unit for Human Resources & Institutional Development, Research and Innovation (grant number B05F640203) and National Research Council of Thailand (NRCT) and Kasetsart University for funding (N42A650277), Thailand.

**Conflicts of Interest:** The authors declare no conflict of interest.

## References

1. Choi, J.-H. Fabrication of a carbon electrode using activated carbon powder and application to the capacitive deionization process. *Sep. Purif. Technol.* **2010**, *70*, 362–366. [CrossRef]
2. Huang, W.; Zhang, Y.; Bao, S.; Cruz, R.; Song, S. Desalination by capacitive deionization process using nitric acid-modified activated carbon as the electrodes. *Desalination* **2014**, *340*, 67–72. [CrossRef]
3. Sarasidis, V.C.; Plakas, K.V.; Karabelas, A.J. Novel water-purification hybrid processes involving in-situ regenerated activated carbon, membrane separation and advanced oxidation. *J. Chem. Eng.* **2017**, *328*, 1153–1163. [CrossRef]
4. Gokce, Y.; Aktas, Z. Nitric acid modification of activated carbon produced from waste tea and adsorption of methylene blue and phenol. *Appl. Surf. Sci.* **2014**, *313*, 352–359. [CrossRef]
5. Pi, K.; Xia, M.; Wu, P.; Yang, M.; Chen, S.; Liu, D.; Gerson, A.R. Effect of oxidative modification of activated carbon for the adsorption behavior of nicotine. *J. Ind. Eng. Chem.* **2015**, *31*, 112–117. [CrossRef]
6. Zhu, G.; Xing, X.; Wang, J.; Zhang, X. Effect of acid and hydrothermal treatments on the dye adsorption properties of biomass-derived activated carbon. *J. Mater. Sci.* **2017**, *52*, 7664–7676. [CrossRef]
7. Eslami, A.; Borghei, S.M.; Rashidi, A.; Takdastan, A. Preparation of activated carbon dots from sugarcane bagasse for naphthalene removal from aqueous solutions. *Sep. Sci. Technol.* **2018**, *53*, 2536–2549. [CrossRef]
8. Feroldi, M.; Neves, A.C.; Borba, C.E.; Alves, H.J. Methane storage in activated carbon at low pressure under different temperatures and flow rates of charge. *J. Clean. Prod.* **2018**, *172*, 921–926. [CrossRef]

9. Sawant, S.Y.; Munusamy, K.; Somani, R.S.; John, M.; Newalkar, B.L.; Bajaj, H.C. Precursor suitability and pilot scale production of super activated carbon for greenhouse gas adsorption and fuel gas storage. *J. Chem. Eng.* **2017**, *315*, 415–425. [CrossRef]
10. Adinaveen, T.; Kennedy, L.J.; Vijaya, J.J.; Sekaran, G. Studies on structural, morphological, electrical and electrochemical properties of activated carbon prepared from sugarcane bagasse. *J. Ind. Eng. Chem.* **2013**, *19*, 1470–1476. [CrossRef]
11. Inal, I.I.G.; Holmes, S.M.; Banford, A.; Aktas, Z. The performance of supercapacitor electrodes developed from chemically activated carbon produced from waste tea. *Appl. Surf. Sci.* **2015**, *357*, 696–703. [CrossRef]
12. Oh, I.; Kim, M.; Kim, J. Deposition of $Fe_3O_4$ on oxidized activated carbon by hydrazine reducing method for high performance supercapacitor. *Microelectron. Reliab.* **2015**, *55*, 114–122. [CrossRef]
13. Su, X.-L.; Chen, J.-R.; Zheng, G.-P.; Yang, J.-H.; Guan, X.-X.; Liu, P.; Zheng, X.-C. Three-dimensional porous activated carbon derived from loofah sponge biomass for supercapacitor applications. *Appl. Surf. Sci.* **2018**, *436*, 327–336. [CrossRef]
14. Zheng, J.; Yan, B.; Feng, L.; Zhang, Q.; Zhang, C.; Yang, W.; Han, J.; Jiang, S.; He, S. Potassium citrate assisted synthesis of hierarchical porous carbon materials for high performance supercapacitors. *Diam. Relat. Mater.* **2022**, *128*, 109247. [CrossRef]
15. Zaidi, N.A.H.M.; Lim, L.B.L.; Usman, A.; Kooh, M.R.R. Efficient adsorption of malachite green dye using Artocarpus odoratissimus leaves with artificial neural network modelling. *Desalin. Water Treat.* **2018**, *101*, 313–324. [CrossRef]
16. Kooh, M.R.R.; Thotagamuge, R.; Chau, Y.-F.C.; Mahadi, A.H.; Lim, C.M. Machine learning approaches to predict adsorption capacity of Azolla pinnata in the removal of methylene blue. *J. Taiwan Inst. Chem. Eng.* **2022**, *132*, 104134. [CrossRef]
17. Obey, G.; Adelaide, M.; Ramaraj, R. Biochar derived from non-customized matamba fruit shell as an adsorbent for wastewater treatment. *J. Bioresour. Bioprod.* **2022**, *7*, 109–115. [CrossRef]
18. Jin, X.; Liang, Y.; Wang, J.; Wang, Q.; Wu, Y.; Chong, W.W.F.; Sonne, C.; Lam, S.S.; Xia, C. Hierarchical self-assembly of polyphenolic functionalized magnetic superstructure for enhanced removal of organic dyes. *J. Chem. Eng.* **2023**, *457*, 141142. [CrossRef]
19. Xia, C.; Li, X.; Wu, Y.; Suharti, S.; Unpaprom, Y.; Pugazhendhi, A. A review on pollutants remediation competence of nanocomposites on contaminated water. *Environ. Res.* **2023**, *222*, 115318. [CrossRef]
20. Boudrahem, F.; Soualah, A.; Aissani-Benissad, F. Pb(II) and Cd(II) removal from aqueous solutions using activated carbon developed from coffee residue activated with phosphoric acid and zinc chloride. *J. Chem. Eng. Data* **2011**, *56*, 1946–1955. [CrossRef]
21. Lozano-Castello, D.; Lillo-Ródenas, M.; Cazorla-Amorós, D.; Linares-Solano, A. Preparation of activated carbons from Spanish anthracite: I. Activation by KOH. *Carbon* **2001**, *39*, 741–749. [CrossRef]
22. Tsai, W.; Chang, C.; Wang, S.; Chang, C.; Chien, S.; Sun, H. Cleaner production of carbon adsorbents by utilizing agricultural waste corn cob. *Resour. Conserv. Recycl.* **2001**, *32*, 43–53. [CrossRef]
23. Zhang, H.; Wang, Y.; Bai, P.; Guo, X.; Ni, X. Adsorptive Separation of Acetic Acid from Dilute Aqueous Solutions: Adsorption Kinetic, Isotherms, and Thermodynamic Studies. *J. Chem. Eng. Data* **2016**, *61*, 213–219. [CrossRef]
24. Mi, J.; Wang, X.-R.; Fan, R.-J.; Qu, W.-H.; Li, W.-C. Coconut-Shell-Based Porous Carbons with a Tunable Micro/Mesopore Ratio for High-Performance Supercapacitors. *Energy Fuels* **2012**, *26*, 5321–5329. [CrossRef]
25. Mohanty, K.; Naidu, J.T.; Meikap, B.C.; Biswas, M.N. Removal of Crystal Violet from Wastewater by Activated Carbons Prepared from Rice Husk. *Ind. Eng. Chem. Res.* **2006**, *45*, 5165–5171. [CrossRef]
26. Sudhan, N.; Subramani, K.; Karnan, M.; Ilayaraja, N.; Sathish, M. Biomass-Derived Activated Porous Carbon from Rice Straw for a High-Energy Symmetric Supercapacitor in Aqueous and Non-aqueous Electrolytes. *Energy Fuels* **2017**, *31*, 977–985. [CrossRef]
27. Khenniche, L.; Benissad-Aissani, F. Adsorptive Removal of Phenol by Coffee Residue Activated Carbon and Commercial Activated Carbon: Equilibrium, Kinetics, and Thermodynamics. *J. Chem. Eng. Data* **2010**, *55*, 4677–4686. [CrossRef]
28. Liu, Q.-S.; Zheng, T.; Li, N.; Wang, P.; Abulikemu, G. Modification of bamboo-based activated carbon using microwave radiation and its effects on the adsorption of methylene blue. *Appl. Surf. Sci.* **2010**, *256*, 3309–3315. [CrossRef]
29. Zhang, Q.; Zeng, Y.; Xiao, X.; Deng, P.; He, Q.; Zhang, T. Investigation on the preparation and adsorption performance of bamboo fiber based activated carbon. *Fibers Polym.* **2019**, *20*, 293–301. [CrossRef]
30. Yang, C.-S.; Jang, Y.S.; Jeong, H.K. Bamboo-based activated carbon for supercapacitor applications. *Curr. Appl. Phys.* **2014**, *14*, 1616–1620. [CrossRef]
31. Taer, E. Preparation of Activated Carbon Electrode from Pineapple Crown Waste for Supercapacitor Application. *Int. J. Electrochem. Sci.* **2019**, *14*, 2462–2475. [CrossRef]
32. Sethupathi, S.; Bashir, M.J.K.; Akbar, Z.A.; Mohamed, A.R. Biomass-based palm shell activated carbon and palm shell carbon molecular sieve as gas separation adsorbents. *Waste Manag. Res.* **2015**, *33*, 303–312. [CrossRef]
33. Onundi, Y.B.; Mamun, A.A.; Khatib, M.F.A.; Ahmed, Y.M. Adsorption of copper, nickel and lead ions from synthetic semiconductor industrial wastewater by palm shell activated carbon. *Int. J. Environ. Sci. Technol.* **2010**, *7*, 751–758. [CrossRef]
34. Budinova, T.; Petrov, N.; Razvigorova, M.; Parra, J.; Galiatsatou, P. Removal of Arsenic(III) from Aqueous Solution by Activated Carbons Prepared from Solvent Extracted Olive Pulp and Olive Stones. *Ind. Eng. Chem. Res.* **2006**, *45*, 1896–1901. [CrossRef]
35. Mohammadi, S.Z.; Karimi, M.A.; Afzali, D.; Mansouri, F. Removal of Pb(II) from aqueous solutions using activated carbon from Sea-buckthorn stones by chemical activation. *Desalination* **2010**, *262*, 86–93. [CrossRef]
36. Köseoğlu, E.; Akmil-Başar, C. Preparation, structural evaluation and adsorptive properties of activated carbon from agricultural waste biomass. *Adv. Powder Technol.* **2015**, *26*, 811–818. [CrossRef]
37. Tao, H.-C.; Zhang, H.-R.; Li, J.-B.; Ding, W.-Y. Biomass based activated carbon obtained from sludge and sugarcane bagasse for removing lead ion from wastewater. *Bioresour. Technol.* **2015**, *192*, 611–617. [CrossRef]

38. Sekirifa, M.L.; Hadj-Mahammed, M.; Pallier, S.; Baameur, L.; Richard, D.; Al-Dujaili, A.H. Preparation and characterization of an activated carbon from a date stones variety by physical activation with carbon dioxide. *J. Anal. Appl. Pyrolysis* **2013**, *99*, 155–160. [CrossRef]
39. Zhou, J.; Luo, A.; Zhao, Y. Preparation and characterisation of activated carbon from waste tea by physical activation using steam. *J. Air Waste Manag. Assoc.* **2018**, *68*, 1269–1277. [CrossRef] [PubMed]
40. Momčilović, M.; Purenović, M.; Bojić, A.; Zarubica, A.; Ranđelović, M. Removal of lead(II) ions from aqueous solutions by adsorption onto pine cone activated carbon. *Desalination* **2011**, *276*, 53–59. [CrossRef]
41. Dong, Q.; Guo, X.; Huang, X.; Liu, L.; Tallon, R.; Taylor, B.; Chen, J. Selective removal of lead ions through capacitive deionization: Role of ion-exchange membrane. *J. Chem. Eng.* **2019**, *361*, 1535–1542. [CrossRef]
42. Asuquo, E.; Martin, A.; Nzerem, P.; Siperstein, F.; Fan, X. Adsorption of Cd(II) and Pb(II) ions from aqueous solutions using mesoporous activated carbon adsorbent: Equilibrium, kinetics and characterisation studies. *J. Environ. Chem. Eng.* **2017**, *5*, 679–698. [CrossRef]
43. Song, M.; Wei, Y.; Cai, S.; Yu, L.; Zhong, Z.; Jin, B. Study on adsorption properties and mechanism of $Pb^{2+}$ with different carbon based adsorbents. *Sci. Total Environ.* **2018**, *618*, 1416–1422. [CrossRef] [PubMed]
44. Soylak, M.; Altin, R. Membrane Filtration of Lead, Cobalt, and Nickel in Water and Fertilizer Samples for Enrichment/Separation and Flame Atomic Absorption Spectrometric Determination. *At. Spectrosc.* **2014**, *35*, 79. [CrossRef]
45. Toosi, M.R.; Emami, M.R.S.; Hajian, S. Dynamic filtration and static adsorption of lead ions in aqueous solution by use of blended polysulfone membranes with nano size MCM-41 particles coated by polyaniline. *Environ. Sci. Pollut. Res.* **2018**, *25*, 20217–20230. [CrossRef] [PubMed]
46. Németh, G.; Mlinárik, L.; Török, Á. Adsorption and chemical precipitation of lead and zinc from contaminated solutions in porous rocks: Possible application in environmental protection. *J. Afr. Earth Sci.* **2016**, *122*, 98–106. [CrossRef]
47. Rabii, A.; Bidhendi, G.N.; Mehrdadi, N. Evaluation of lead and COD removal from lead octoate drier effluent by chemical precipitation, coagulation–flocculation, and potassium persulfate oxidation processes. *Desalin. Water Treat.* **2012**, *43*, 1–7. [CrossRef]
48. Şahin, Ö.; Saka, C. Preparation and characterization of activated carbon from acorn shell by physical activation with $H_2O$–$CO_2$ in two-step pretreatment. *Bioresour. Technol.* **2013**, *136*, 163–168. [CrossRef]
49. DOE/NE-ID-11173 FreedomCAR Capacitor Test Manual. 21 September 2004. Available online: https://avt.inl.gov/sites/default/files/pdf/battery/FreedomCAR_Capacitor_Test_Manual_Sept_2004.pdf (accessed on 1 February 2023).
50. Liew, R.K.; Chong, M.Y.; Osazuwa, O.U.; Nam, W.L.; Phang, X.Y.; Su, M.H.; Cheng, C.K.; Chong, C.T.; Lam, S.S. Production of activated carbon as catalyst support by microwave pyrolysis of palm kernel shell: A comparative study of chemical versus physical activation. *Res. Chem. Intermed.* **2018**, *44*, 3849–3865. [CrossRef]
51. Cychosz, K.A.; Thommes, M. Progress in the Physisorption Characterization of Nanoporous Gas Storage Materials. *Engineering* **2018**, *4*, 559–566. [CrossRef]
52. Moreno-Tovar, R.; Terrés, E.; Rangel-Mendez, J.R. Oxidation and EDX elemental mapping characterization of an ordered mesoporous carbon: Pb(II) and Cd(II) removal. *Appl. Surf. Sci.* **2014**, *303*, 373–380. [CrossRef]
53. Angin, D. Production and characterization of activated carbon from sour cherry stones by zinc chloride. *Fuel* **2014**, *115*, 804–811. [CrossRef]
54. Song, X.; Liu, H.; Cheng, L.; Qu, Y. Surface modification of coconut-based activated carbon by liquid-phase oxidation and its effects on lead ion adsorption. *Desalination* **2010**, *255*, 78–83. [CrossRef]
55. Mouni, L.; Merabet, D.; Bouzaza, A.; Belkhiri, L. Adsorption of Pb(II) from aqueous solutions using activated carbon developed from Apricot stone. *Desalination* **2011**, *276*, 148–153. [CrossRef]
56. Menya, E.; Olupot, P.; Storz, H.; Lubwama, M.; Kiros, Y. Production and performance of activated carbon from rice husks for removal of natural organic matter from water: A review. *Chem. Eng. Res. Des.* **2018**, *129*, 271–296. [CrossRef]
57. Jjagwe, J.; Olupot, P.W.; Menya, E.; Kalibbala, H.M. Synthesis and Application of Granular Activated Carbon from Biomass Waste Materials for Water Treatment: A Review. *J. Bioresour. Bioprod.* **2021**, *6*, 292–322. [CrossRef]
58. Sarada, B.; Prasad, M.K.; Kumar, K.K.; Murthy, C.V.R. Cadmium removal by macro algae *Caulerpa fastigiata*: Characterization, kinetic, isotherm and thermodynamic studies. *J. Environ. Chem. Eng.* **2014**, *2*, 1533–1542. [CrossRef]
59. El-Hendawy, A.-N.A. An insight into the KOH activation mechanism through the production of microporous activated carbon for the removal of $Pb^{2+}$ cations. *Appl. Surf. Sci.* **2009**, *255*, 3723–3730. [CrossRef]
60. Alkherraz, A.M.; Ali, A.K.; Elsherif, K.M. Removal of Pb(II), Zn(II), Cu(II) and Cd(II) from aqueous solutions by adsorption onto olive branches activated carbon: Equilibrium and thermodynamic studies. *Chem. Int.* **2020**, *6*, 11–20.
61. Neolaka, Y.A.B.; Lawa, Y.; Naat, J.; Riwu, A.A.P.; Darmokoesoemo, H.; Widyaningrum, B.A.; Iqbal, M.; Kusuma, H.S. Indonesian Kesambi wood (*Schleichera oleosa*) activated with pyrolysis and $H_2SO_4$ combination methods to produce mesoporous activated carbon for Pb(II) adsorption from aqueous solution. *Environ. Technol. Innov.* **2021**, *24*, 101997. [CrossRef]
62. Thabede, P.M.; Shooto, N.D.; Naidoo, E.B. Removal of methylene blue dye and lead ions from aqueous solution using activated carbon from black cumin seeds. *S. Afr. J. Chem. Eng.* **2020**, *33*, 39–50. [CrossRef]
63. Roberts, A.J.; Slade, R.C. Effect of specific surface area on capacitance in asymmetric carbon/$\alpha$-$MnO_2$ supercapacitors. *Electrochim. Acta* **2010**, *55*, 7460–7469. [CrossRef]
64. Zhang, S.; Pan, N. Supercapacitors performance evaluation. *Adv. Energy Mater.* **2015**, *5*, 1401401. [CrossRef]

65. Li, X.-R.; Jiang, Y.-H.; Wang, P.-Z.; Mo, Y.; Li, Z.-J.; Yu, R.-J.; Du, Y.-T.; Zhang, X.-R.; Chen, Y. Effect of the oxygen functional groups of activated carbon on its electrochemical performance for supercapacitors. *New Carbon Mater.* **2020**, *35*, 232–243.
66. Yuan, S.; Huang, X.; Wang, H.; Xie, L.; Cheng, J.; Kong, Q.; Sun, G.; Chen, C.-M. Structure evolution of oxygen removal from porous carbon for optimizing supercapacitor performance. *J. Energy Chem.* **2020**, *51*, 396–404. [CrossRef]
67. Köse, K.Ö.; Pişkin, B.; Aydınol, M.K. Chemical and structural optimization of $ZnCl_2$ activated carbons via high temperature $CO_2$ treatment for EDLC applications. *Int. J. Hydrogen Energy* **2018**, *43*, 18607–18616. [CrossRef]
68. Mei, B.-A.; Munteshari, O.; Lau, J.; Dunn, B.; Pilon, L. Physical Interpretations of Nyquist Plots for EDLC Electrodes and Devices. *J. Phys. Chem. C* **2017**, *122*, 194–206. [CrossRef]
69. Zhao, J.; Burke, A.F. Electrochemical capacitors: Performance metrics and evaluation by testing and analysis. *Adv. Energy Mater.* **2021**, *11*, 2002192. [CrossRef]
70. Maxwell Technologies Datasheet, 3003279-EN.3, 2.7V 3000F ULTRACAPACITOR CELL. Available online: https://maxwell.com/products/ultracapacitors/downloads/ (accessed on 1 February 2023).


**Disclaimer/Publisher's Note:** The statements, opinions and data contained in all publications are solely those of the individual author(s) and contributor(s) and not of MDPI and/or the editor(s). MDPI and/or the editor(s) disclaim responsibility for any injury to people or property resulting from any ideas, methods, instructions or products referred to in the content.